RSC Advances

PAPER

View Article Online
View Journal | View Issue

Cite this: *RSC Adv.*, 2026, **16**, 17437

Sensitive and selective $NiFe_2O_4$-based gas sensor for hazardous hydrogen sulfide (H_2S) monitoring

Ibtihel Soudani, *[a] Rageh K. Hussein,[b] Saja Algessair,[b] K. Moulae,[c] Mokhtar Hjiri *[b] and Giovanni Neri[c]

Hydrogen sulfide (H_2S) is a hazardous environmental pollutant that poses significant health risks, demanding the development of high-performance monitoring systems. This work reports the successful hydrothermal synthesis of inverse spinel nickel ferrite $NiFe_2O_4$ nanomaterials for use as a chemiresistive gas sensor. Structural and morphological characterizations, such as X-ray diffraction (XRD), scanning electron microscopy (SEM), Transmission electron microscopy (TEM), and photoluminescence (PL), confirmed the formation of a cubic spinel phase with a mesoporous architecture. Brunauer–Emmett–Teller (BET) analysis revealed a specific surface area of 58 $m^2\ g^{-1}$, which provides an abundance of active sites for gas–solid interactions. X-ray photoelectron spectroscopy (XPS) analysis elucidated the sensing mechanism, showing the appearance of sulfur species and shifts in Ni 2p peaks, confirming the strong interaction between H_2S and the ferrite surface. The sensing performance was systematically evaluated, showing a remarkable response of 90 toward a low H_2S concentration of 5 ppm at an optimal operating temperature of 200 °C. This detection capability is well below the Threshold Limit Value (10 ppm). The sensor exhibited a quick response time of 10 seconds, exceptional selectivity, and high stability, demonstrated by a low relative standard deviation (RSD of 1.12%). Although humidity caused competitive adsorption effects, the sensor maintained a strong and measurable signal. These results indicate that $NiFe_2O_4$ is an excellent candidate for sensitive and practical H_2S detection applications.

Received 14th January 2026
Accepted 26th March 2026

DOI: 10.1039/d6ra00366d

rsc.li/rsc-advances

1. Introduction

Hydrogen sulfide (H_2S) is a colorless, flammable, and highly toxic gas widely encountered in petroleum refining, wastewater treatment, and natural gas processing.[1–4] Even at low concentrations, H_2S exposure can irritate the eyes and respiratory system, while prolonged exposure may lead to severe neurological damage or fatal outcomes.[5] According to occupational safety standards, the threshold limit value (TLV) of H_2S is 10 ppm for an 8 hour time-weighted average exposure, highlighting the need for reliable detection systems capable of operating at sub-ppm levels.[5]

Chemiresistive gas sensors based on semiconducting metal oxides have attracted significant attention due to their low cost, simplicity, and high sensitivity. Conventional materials such as ZnO, SnO_2, TiO_2, and CuO have been widely explored for H_2S detection.[6–8] However, these materials often suffer from limitations such as high operating temperatures, poor selectivity, and slow response/recovery dynamics, which restrict their practical deployment.[9–12]

Recently, spinel ferrites (AB_2O_4) have emerged as promising candidates for gas-sensing applications due to their tunable electrical conductivity, catalytic activity, and structural flexibility.[13,14] The spinel structure consists of tetrahedral (A) and octahedral (B) sites, enabling control over cation distribution and charge transport mechanisms. In particular, electron hopping between mixed valence states (*e.g.*, Fe^{2+}/Fe^{3+}) plays a crucial role in determining their sensing behavior.[15,16]

Nickel ferrite ($NiFe_2O_4$), an inverse spinel ferrite, has attracted considerable interest owing to its semiconducting nature, chemical stability, and strong interaction with sulfur-containing gases.[17] Recent studies have demonstrated the potential of nanostructured $NiFe_2O_4$ for gas sensing applications. For instance, electrospun $NiFe_2O_4$ nanofibers exhibited sensitivity toward H_2S; however, they required relatively high operating temperatures (~350 °C) and showed moderate response values.[18,19] Furthermore, recent advances have focused on enhancing sensing performance through morphology engineering and composite formation. For example, $MgFe_2O_4/MoO_3$ nanocomposites showed improved response at lower temperatures (135 °C), attributed to increased surface area and heterojunction effects.[20] Despite these advances, several limitations persist in ferrite-based sensors. Many reported systems require complex synthesis routes, incorporation of

[a]*Laboratory of Multifunctional Materials and Applications (LaMMA), LR16ES18, Faculty of Sciences of Sfax, University of Sfax, BP 1171, 3000 Sfax, Tunisia. E-mail: ebtihel.soudani@gmail.com*

[b]*Department of Physics, College of Sciences, Imam Mohammad Ibn Saud Islamic University (IMSIU), Riyadh 11623, Saudi Arabia. E-mail: mbhjiri@imamu.edu.sa*

[c]*Department of Engineering, University of Messina, Messina 98166, Italy*

secondary phases, or operate at relatively high temperatures to achieve acceptable sensitivity.[13,21,22] In addition, achieving simultaneous improvement in detection limit, response time, and selectivity remains a major challenge. Recently, various strategies have been developed for hydrogen sulfide detection, including portable colorimetric systems for environmental monitoring, surface-enhanced Raman scattering (SERS)-based methods, and visual detection techniques.[23–25] These approaches offer high sensitivity and suitability for on-site analysis; however, they often suffer from limitations such as complex instrumentation, high cost, or limited real-time capability. In contrast, chemiresistive gas sensors based on metal oxides provide a simple, low-cost, and real-time detection approach, making them highly promising for practical applications.[26,27]

Compared with previously reported $NiFe_2O_4$-based sensors, which often require high operating temperatures or exhibit moderate sensitivity, there remains a need for simple, single-phase nanostructured materials capable of detecting H_2S at low concentrations with fast response and high selectivity.[17–19] Therefore, the key scientific challenge is to develop $NiFe_2O_4$-based sensors that combine low detection limit, rapid response, high selectivity, and reduced operating temperature, without relying on complex doping strategies or composite structures. One effective approach to address this challenge is the design of nanostructured materials with reduced particle size and porous morphology. Nanoscale materials offer a high surface-to-volume ratio, enhanced density of active sites, and shorter diffusion pathways for gas molecules. In addition, surface defects such as oxygen vacancies play a crucial role in gas sensing by facilitating oxygen adsorption and promoting surface reactions. Despite extensive studies on $NiFe_2O_4$-based H_2S sensors, a comprehensive understanding linking defect states, surface chemistry, and environmental factors to sensing performance remains limited. In this work, we address this gap by combining PL, BET, and XPS analyses with gas sensing measurements to provide a deeper insight into the sensing mechanism and practical applicability.

2. Experiments

2.1. Preparation of $NiFe_2O_4$ nanopowders

The hydrothermal technique has been utilized to synthesize nickel ferrite nanoparticles with a Ni load of 25 at%. Nickel salt ($NiCl_2$) and iron salt ($FeCl_3$) were the starting materials. Distilled water was used to dissolve the two salts using a magnetic stirrer. To get a basic medium, a quantity of ammonium hydroxide (2 ml) is dropped into the solution. The obtained solution was placed in a Teflon-lined steel autoclave and heated at 200 °C for 6 hours. The obtained materials were repeatedly washed with ethanol and water, followed by drying at 60 °C for 1 hour. A calcination for 2 hours at 500 °C is necessary for the crystallization of the elaborated powders.

2.2. Sample characterizations

Nickel ferrite nanopowder was characterized using a Bruker D8 Advance X-ray diffractometer (Germany) at 40 kV and 40 mA, with Cu Kα radiation ($\lambda = 0.154056$ nm), scanning from 20° to 70° in 2θ. Scanning electron microscopy (JEOL JSM-7600F) assessed sample morphology, while specific surface area and pore size distribution were measured *via* N_2 adsorption–desorption isotherms using BET and BJH methods. The transmission electron microscopy (JEOL JEM-200F) evaluated particle size and shape. X-ray photoelectron spectroscopy (XPS) determined the valence states of elements in the samples. The photoluminescence (PL) was carried out on a NanoLog modular spectrofluorometer Horiba with a Xe lamp as the excitation light source at ambient temperature.

2.3. Gas sensing performances

Sensors were made by pasting thick films (1–10 μm) of the powders mixed with water on alumina substrates. Electrical contacts were made using silver paste deposited on the sensing layer, followed by drying to ensure good electrical conductivity. To perform detection tests, sensors were then placed in a stainless steel test chamber. The temperature of electrical measurements and sensing tests ranged from 150 to 400 °C. Target gases derived from authenticated bottles might be diluted more in air at a suggested concentration using mass flow controllers. Hydrogen sulfide concentration ranged from 0.126 to 5.04 ppm. To control sensing layer resistance, a multimeter data acquisition unit (type Agilent 34970A) was used, while a power supply device (type Agilent E3632A) is needed to make measurements at different temperatures. The H_2S sensor response, S, is known as the ratio of the resistance in air (R_a) to the resistance when gas is exposed (R_g).

3. Results and discussion

3.1. X-ray diffraction analysis

Fig. 1 depicts the XRD spectrum of $NiFe_2O_4$ powder synthesized by hydrothermal. The XRD pattern contained diffraction peaks located at 2θ = 30.2°, 35.4°, 37.13°, 43.21°, 53.63°, 57.11°, 62.71°, corresponding to (220), (311), (222), (400), (422), (511), and (440), respectively.

Fig. 2 shows the Rietveld refinement analysis performed with Match software to determine precise structural parameters. Table 1 lists the refined lattice parameters and crystallographic data. The $NiFe_2O_4$ diffraction peaks correspond to a cubic crystal structure (space group $Fd\bar{3}m$,[28,29]), with no extraneous phases indicating sample purity. The refined lattice parameter is $a = 8.3597$ Å, and density measurements yield 2.757 g cm^{-3} for nickel ferrite.

The average crystallite size was estimated using the Scherer formula and the Williamson–Hall relation. Scherer's formula relates the average crystallite size (D_s) to the FWHM (β), wavelength (λ), and the angle (θ) as follows:[30]

$$D_s = \frac{k\lambda}{\beta \cos \theta} \quad (1)$$

The average crystallite size (D_{WH}) and microstrain (ε) effects on the peak broadening were also estimated from the slope and

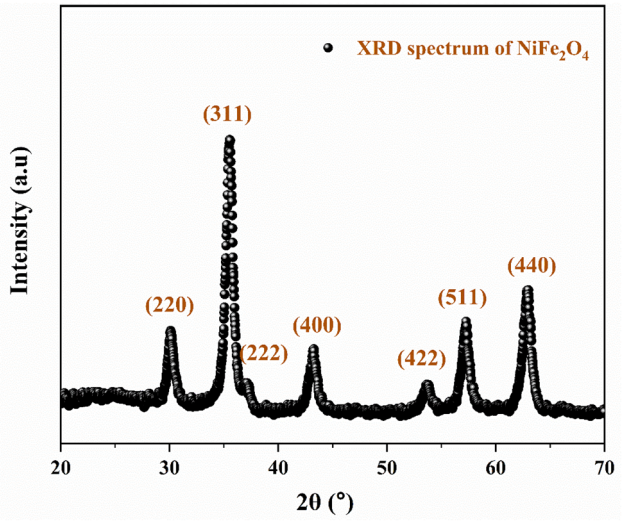

Fig. 1 X-ray diffraction patterns of $NiFe_2O_4$ nanopowders.

y-intercept of the linear fitting result, as shown in Fig. 3, of the Williamson–Hall relation:[31]

$$\beta \cos \theta = 4\varepsilon \sin \theta + \frac{k\lambda}{D_{WH}} \quad (2)$$

The lattice strain and the average crystallite size of nickel ferrite nanomaterial estimated using both methods are displayed in Table 2. The calculated crystallite size using the two methods was almost the same (around 10 nm). The value of lattice strain is found to be negative, indicating that the material was compressed relative to its equilibrium state due to external stresses, defects, or mismatches in the material.[32,33]

Table 1 Parameters deduced from Rietveld analysis

Parameter	Ni Fe_2O_4
Space group	$Fd\bar{3}m$
Crystal system	Cubic
Density (g cm^{-3})	2.757
Lattice parameters, *a* (Å)	8.3597

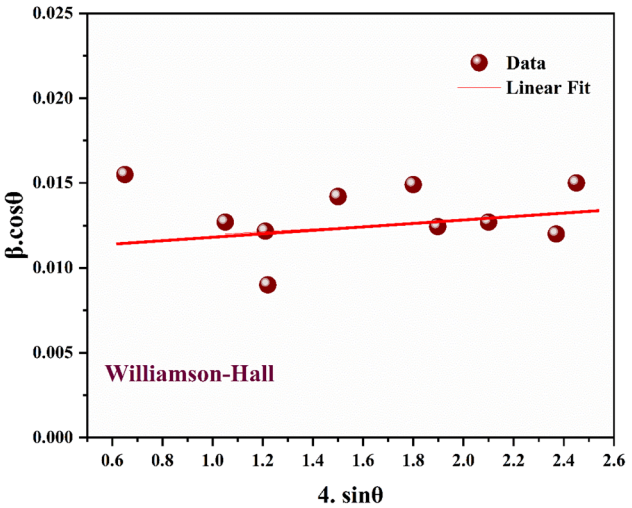

Fig. 3 Williamson–Hall plots of $NiFe_2O_4$ material.

The reliability of semiconductor materials with electrical and optical properties is connected to their structures. The elastic strain field and tilt analysis of the crystal lattice, detectable by the variation in position and shape of the diffraction peaks, is used to quantify defects and investigate their mobility. The

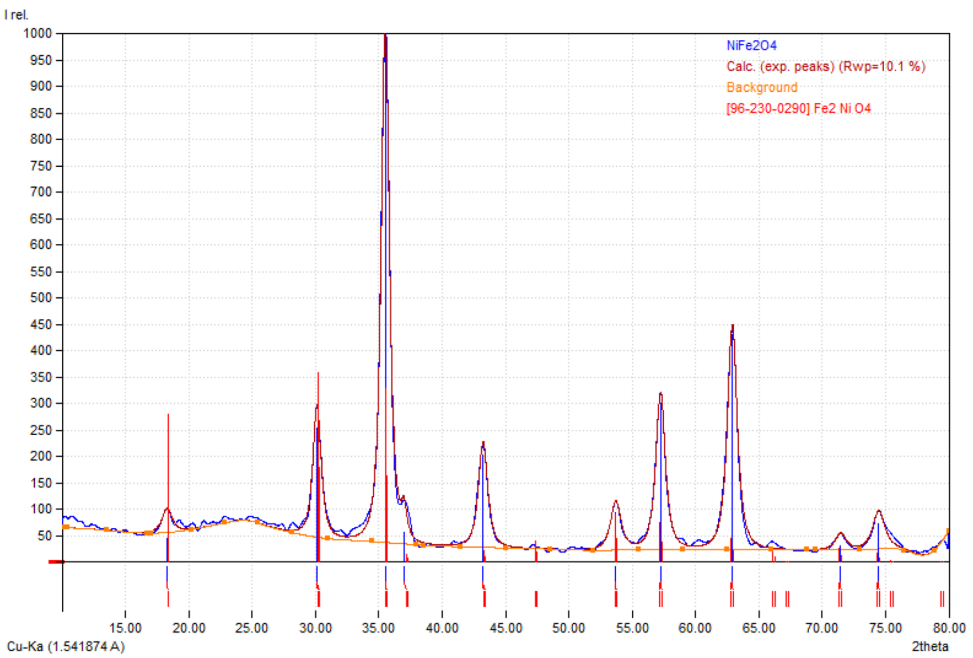

Fig. 2 Rietveld refinement plot of $NiFe_2O_4$ (the blue carve represent the observed data and the burgundy color is the calculated pattern).

Table 2 Average crystallites size and lattice strain (ε)

Parameter	Ni Fe_2O_4
DS (nm)	10.63
DWH (nm)	10.36
Lattice strain ε	-7.027×10^{-8}

exploitation of high-resolution X-ray diffraction-based methods for the evaluation of structural defects in semiconductor materials and devices is reviewed. An efficient and non-destructive characterization is possible for structural parameters such as lattice strain and tilt, layer composition and thickness, lattice mismatch, and dislocation density. The description of specific experimental diffraction geometries and scanning methods is provided. Today's X-ray diffraction-based methods are evaluated and compared, also with respect to their applicability limits. The goal is to understand the close relationship between lattice strain and structural defects. For different material systems, the appropriate analytical methods are highlighted.[32]

3.2. Morphological properties

SEM images and EDX spectroscopy of the materials are depicted in Fig. 4. $NiFe_2O_4$ nanopowder is composed of agglomerations of spherical particles with the presence of a space between them, confirming the porous nature of the material. EDX proves the presence of the main elements (iron, nickel, and oxygen), in addition to the carbon element considered as a contaminant.

The textural properties of $NiFe_2O_4$ nanoparticles were investigated by nitrogen (N_2) adsorption–desorption as represented in Fig. 5. The isotherm exhibits typical type IV behavior with a marked hysteresis loop, indicating the mesoporous nature of the material. The specific surface area, calculated by the BET method, is 58 $m^2\ g^{-1}$. The pore size distribution,

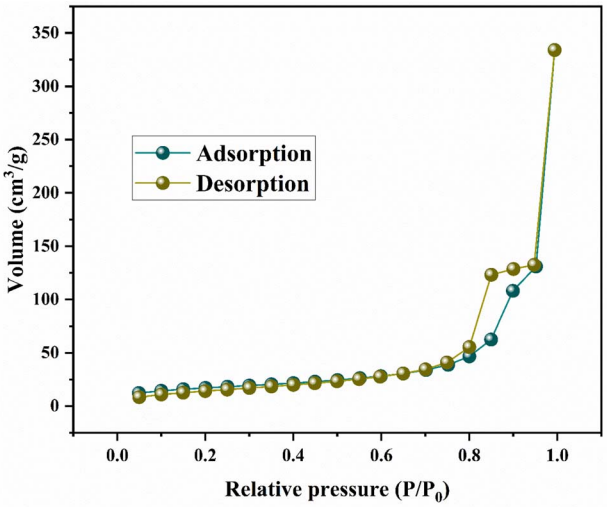

Fig. 5 BET spectra of $NiFe_2O_4$.

determined by the BJH method, confirms the presence of mesopores.[34] The relatively high specific surface area and the porous structure provide a large number of active sites for gas adsorption and facilitate the efficient diffusion of H_2S molecules. These characteristics contribute significantly to improved detection performance, particularly the high response time and the speed of both the response and the recovery.[35]

Fig. 6 displayed TEM photographs of the $NiFe_2O_4$ compound. The nickel ferrite consists of nanoparticles with irregular spherical shapes and significant agglomeration (Fig. 6a). Particle size distribution was determined from TEM images using image analysis software, by measuring individual nanoparticle diameters and generating a histogram of frequency *versus* size, as represented in Fig. 6b. The size distribution showed that the average particle size of $NiFe_2O_4$

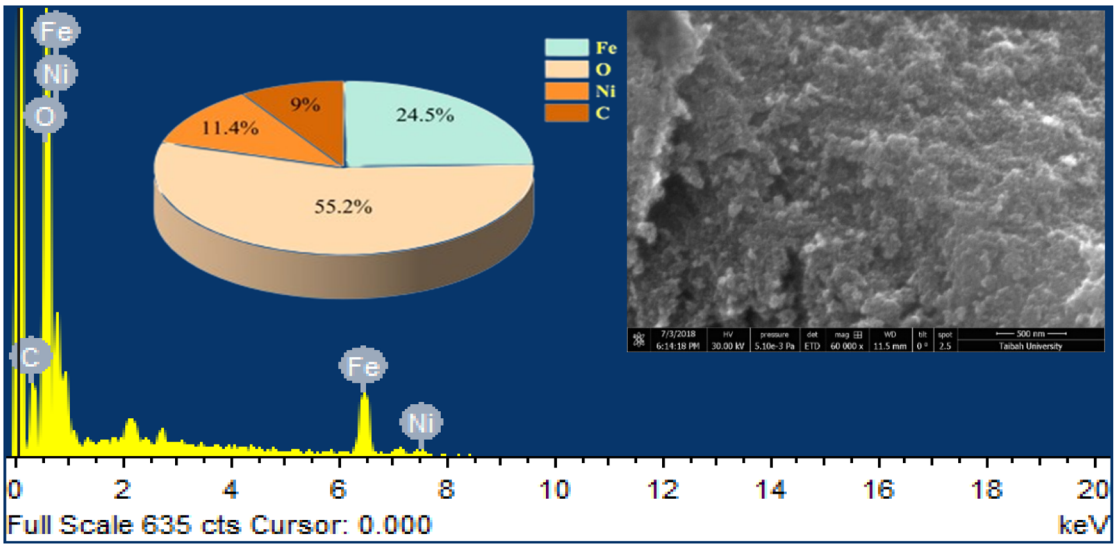

Fig. 4 SEM images and EDX spectrum of $NiFe_2O_4$ material.

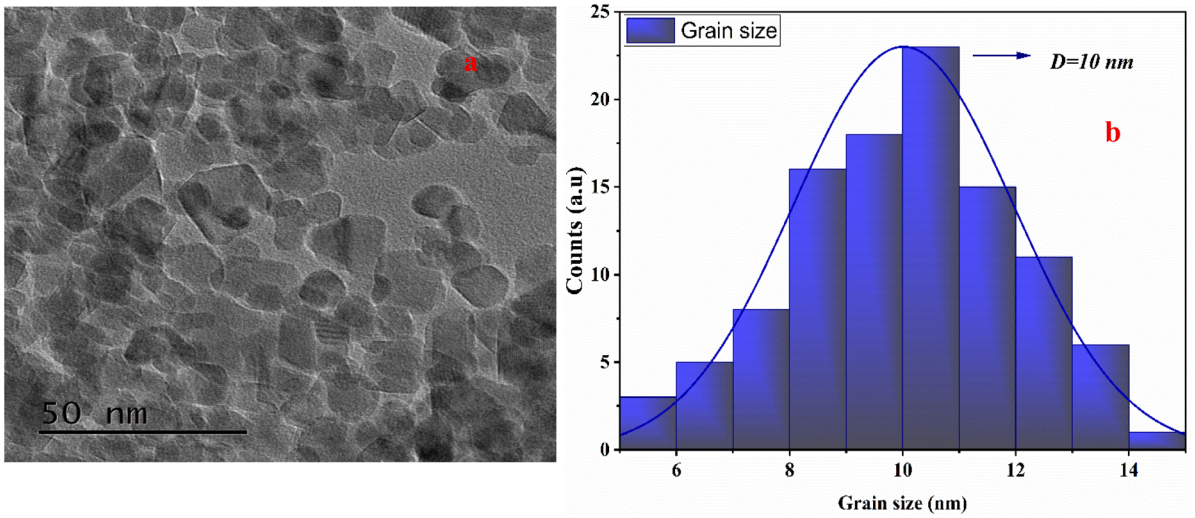

Fig. 6 (a) TEM images and (b) particle size distribution histogram of $NiFe_2O_4$ material.

material (D) is found to be 10 nm. The obtained size was in good agreement with that obtained by XRD measurements.

3.3. XPS analysis

X-ray photoelectron spectroscopy (XPS) was employed to investigate the surface chemical composition and electronic states of $NiFe_2O_4$ before and after exposure to H_2S gas, as showin Fig. 7. The survey spectra confirm the presence of Ni, Fe, and O elements in the pristine sample, while an additional S signal appears after H_2S exposure, indicating the successful adsorption of sulfur-containing species on the sensor surface.

The high-resolution Ni 2p spectrum of the pristine $NiFe_2O_4$ exhibits characteristic peaks corresponding to Ni^{2+} species, along with their associated satellite peaks, confirming the spinel structure (Fig. 7a). After exposure to H_2S, a slight shift of the Ni 2p peaks toward lower binding energy is observed, suggesting an increase in electron density around Ni ions (Fig. 7b). This shift can be attributed to the reducing nature of H_2S gas and indicates a modification of the local chemical environment due to the interaction between Ni ions and sulfur species.[36,37]

The Fe 2p spectrum shows typical features of Fe^{3+} ions in the spinel lattice (Fig. 7c), and no significant shift is observed after gas exposure (Fig. 7f), indicating that Fe plays a less dominant role in the sensing reaction compared to Ni sites.

The O 1s spectrum can be deconvoluted into two main components: lattice oxygen (O^{2-}) at lower binding energy and adsorbed oxygen species (O^-, O_2^-) at higher binding energy (Fig. 7d). After exposure to H_2S, a noticeable decrease in the intensity of the adsorbed oxygen component is observed, indicating the consumption of chemisorbed oxygen species during the sensing reaction (Fig. 7g). This observation supports the widely accepted mechanism in which H_2S reacts with surface oxygen species, releasing electrons back to the conduction band.[38,39]

Importantly, the appearance of S 2p peaks after H_2S exposure, shown in Fig. 7e, provides direct evidence of the interaction between the target gas and the sensor surface. The S 2p spectrum typically shows contributions corresponding to sulfide species (S^{2-}) and oxidized sulfur species (such as SO_x), confirming that H_2S undergoes surface reactions rather than simple physical adsorption.[40]

Based on these observations, the sensing mechanism can be described as a surface-controlled redox process. In air, oxygen molecules adsorb on the surface and capture electrons to form ionized oxygen species, creating an electron depletion layer and increasing resistance. Upon exposure to H_2S, these oxygen species react with H_2S molecules, leading to the formation of sulfur-containing species and the release of electrons back into the conduction band, resulting in a decrease in resistance.[38,39] The XPS results provide strong experimental support for this mechanism, particularly highlighting the role of Ni active sites and surface oxygen species in the gas sensing process.

3.4. Optical properties

The photoluminescence (PL) spectrum of $NiFe_2O_4$ nanoparticles (Fig. 8) provides insight into the electronic structure and defect states within the material. The spectrum exhibits emission bands centered around ~538 nm and ~568 nm. The emission near 568 nm (≈2.18 eV) can be attributed to band-to-band or near band–edge transitions, consistent with reported band gap values of $NiFe_2O_4$. The additional emission features are associated with defect-related states, particularly oxygen vacancies and cation disorder, which introduce localized energy levels within the band gap.[41]

The relatively high PL intensity is consistent with the nanoscale particle size (~10 nm), where quantum confinement and surface effects become significant. The presence of defect states revealed by PL analysis plays a crucial role in gas sensing performance. In particular, oxygen vacancies act as active sites for oxygen adsorption, promoting the formation of reactive oxygen species (O_2^-, O^-) on the surface.[42]

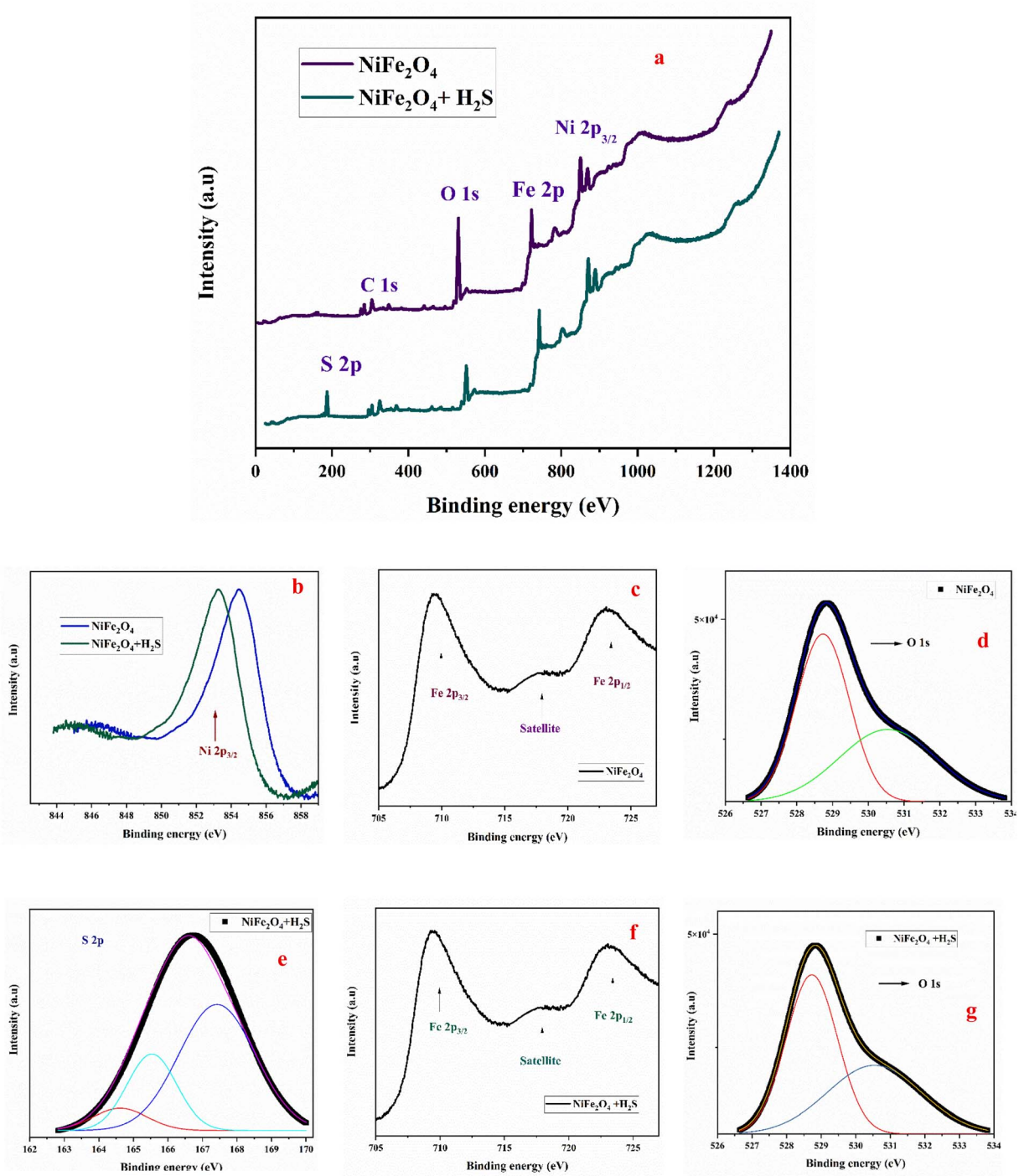

Fig. 7 XPS survey spectra of $NiFe_2O_4$ before and after exposure to H_2S gas (a), high-resolution XPS spectra of the elements of $NiFe_2O_4$ such as Ni (b), Fe (c and f), O (d and g), S (e).

These adsorbed oxygen species capture electrons from the conduction band, leading to the formation of a surface depletion layer and an increase in resistance in air. Upon exposure to H_2S, the gas molecules react with the adsorbed oxygen species, releasing electrons back into the conduction band and decreasing the resistance. Therefore, the defect states evidenced by PL measurements indirectly support the proposed sensing mechanism and contribute to the enhanced sensitivity of the $NiFe_2O_4$ sensor.[43]

3.5. Electric properties

The variation of nickel ferrite resistance as a function of the operating temperature was displayed in Fig. 9. At low temperature (T = 150 °C), the suggested sample exhibited higher electric resistance (about 230 MΩ). Raising the temperature

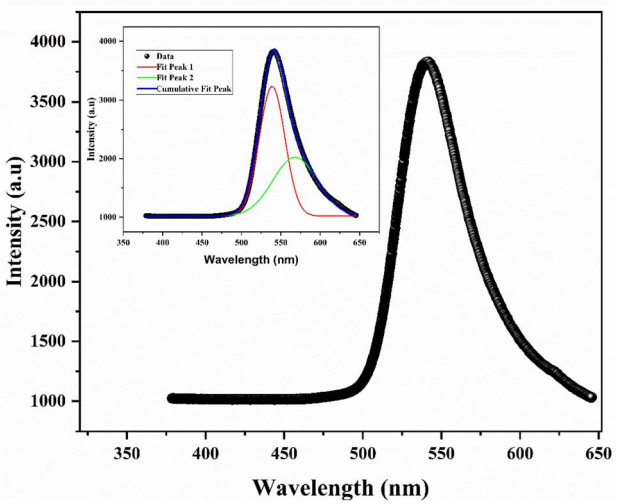

Fig. 8 Photoluminescence spectrum of $NiFe_2O_4$ nanopowders. The inset is a typical deconvolution result of nickel ferrite.

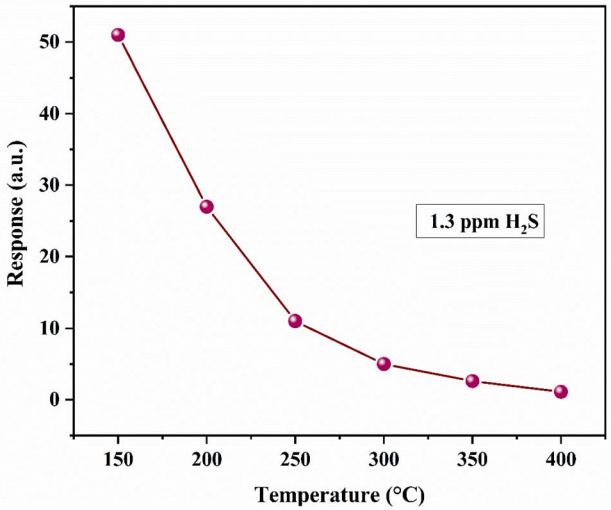

Fig. 10 Variation of gas response toward 1.3 ppm of H_2S *versus* working temperature.

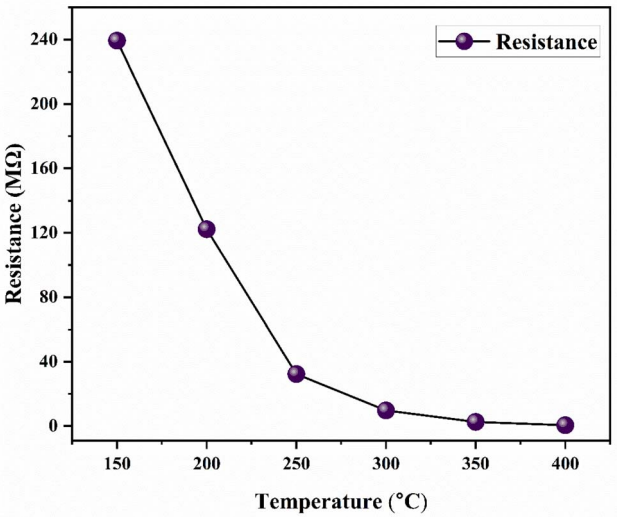

Fig. 9 Variation of resistance *versus* working temperature of $NiFe_2O_4$ material.

results in a reduction of the resistance, indicating the semiconductor behavior of the material. This could be because of the electrons' thermal excitation into the conduction band.

3.6. H_2S gas sensing performances

Since the working temperature was an important factor that influenced the sensitivity, the response-temperature variation of the $NiFe_2O_4$ sensor toward 1.3 ppm of H_2S gas was suggested in Fig. 10. At T = 150 °C, the fabricated sensor achieved a maximum value of 51. Although the maximum response was observed at 150 °C, the sensor exhibited slower response–recovery dynamics and less stable behavior at this temperature. At 200 °C, a better compromise between sensitivity, response speed, and stability was achieved due to enhanced adsorption–desorption kinetics. Therefore, 200 °C was selected as the optimal operating temperature for subsequent measurements. The maximum response indicated that the temperature was enough for gas-adsorbed oxygen species interaction since the rise of thermal energy of gas molecules overcomes the activation energy barrier of the surface reaction with adsorbed oxygen anions.[44,45] Another reason for the higher sensitivity was the increase in the number of free electrons because of the adsorbed oxygen species conversion to O^-.[42] With the increase in temperature, the gas response began to decrease. This behavior might be attributed to the gas adsorption ability reduction for the higher temperatures.[46]

It was clearly seen in Fig. 11 that the fabricated sensor was sensitive to the target gas even at low gas concentrations ($S = 1.5$ toward 0.126 ppm). Furthermore, an increase in H_2S concentration from 0.126 to 5.04 ppm results in a greater decrease in the material's electric resistance. Since H_2S is considered a reducing gas, it then resulted from its interaction with adsorbed oxygen species a loss of electrons leading to conductivity increase and a resistance decrease of the sensing layer, indicating the n-type behavior of the suggested material. The resistances had good reversibility during the exposure and exhaust cycles of H_2S gas.

The response/recovery characteristics curve of the $NiFe_2O_4$ sensor toward 0.315 ppm of hydrogen sulfide gas at the operating temperature of 200 °C is displayed in Fig. 12. When the gas molecules are passed in the test chamber, a sharp decrease in resistance was observed at first, indicating the high response capability; then a slow reduction in resistance appeared until it became constant. On exhausting the gas from the test chamber by opening the valve, the electric resistance increased quickly and then slowly until it reached a constant resistance value in the air for another period of time. The high recovery might be due to the bulk nature of the sensor element. The gas response to 0.315 ppm of H_2S is found to be 4.9.

The response/recovery times are considered the main parameters to say that the sensor is good and efficient. The

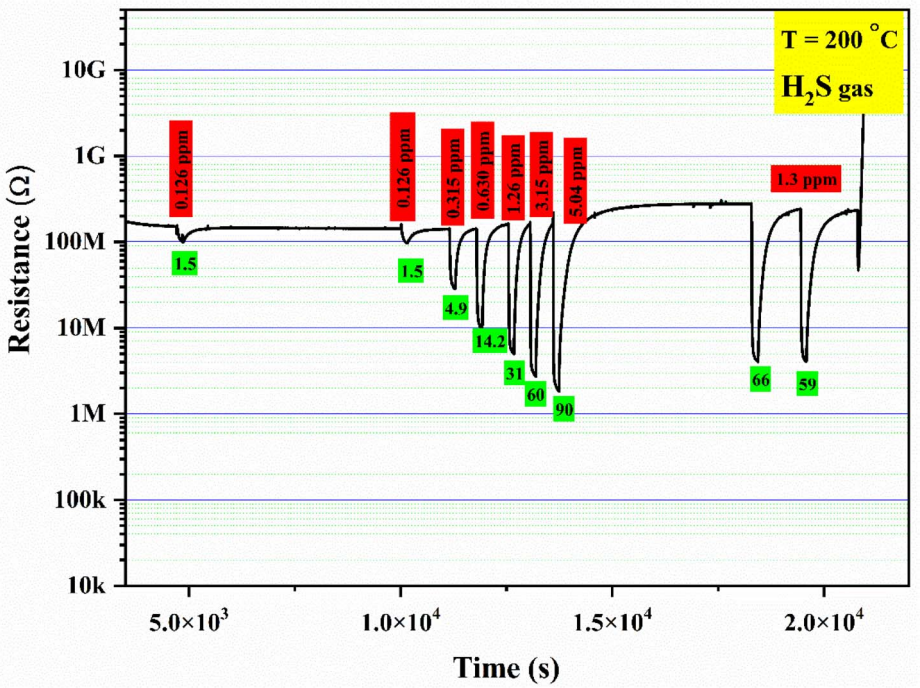

Fig. 11 Resistance-gas concentration dependence of $NiFe_2O_4$ sensor at 200 °C.

response time is defined as the necessary time to obtain 90% of the response when the material is exposed to the gas, while the recovery time is the necessary time for resistance to return to its initial value of 90% when the gas is stopped. The response and recovery are found to be 10 and 170 s, respectively. Ghosh *et al.* obtained response and recovery times of 90 and 300 s when the $NiFe_2O_4$ sensor is exposed to 200 ppm of H_2S.[47]

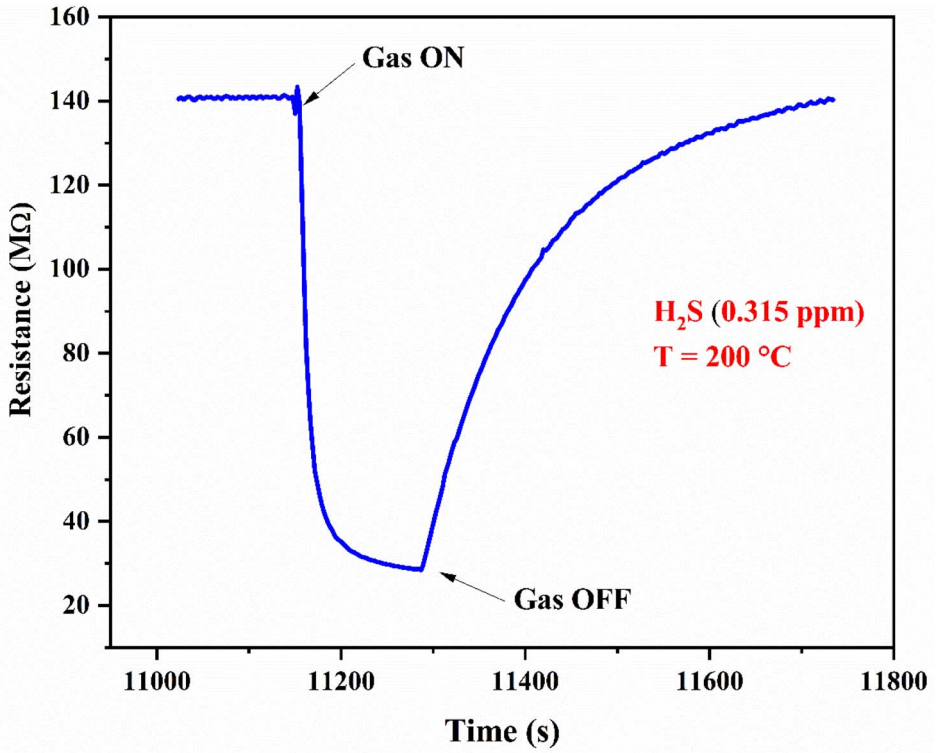

Fig. 12 Electric resistance change with time of nickel ferrite sensor exposed to 0.315 ppm of H_2S at 200 °C.

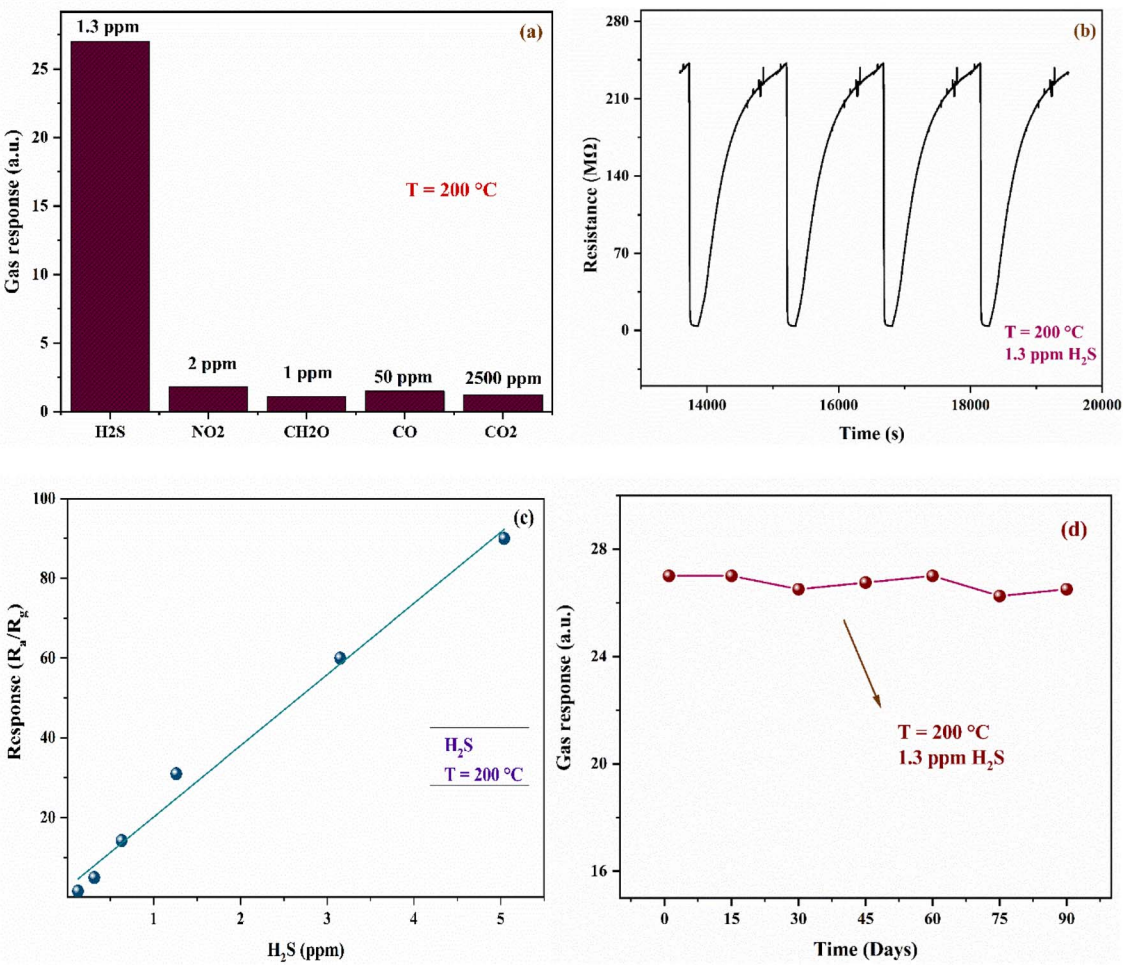

Fig. 13 (a) $NiFe_2O_4$ selectivity test, (b) repeatability test, (c) calibration curve and (d) stability of the sensor during 3 months.

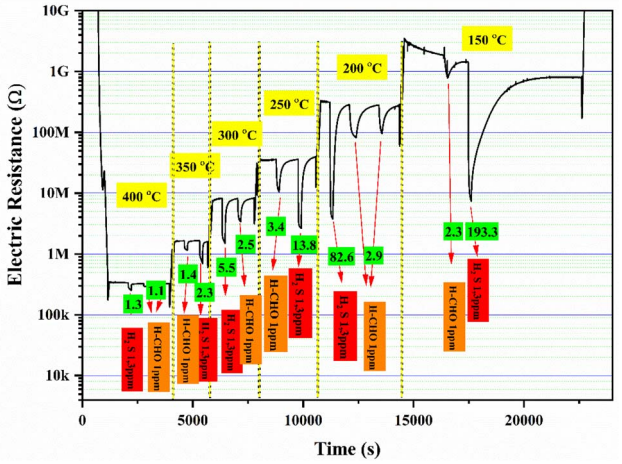

Fig. 14 Dynamic response of $NiFe_2O_4$ sensor toward H_2S and formaldehyde at various temperatures.

The gas response of the $NiFe_2O_4$ sensor toward various gases (CH_2O, CO_2, NO_2, CO, and H_2S) to show its selectivity is depicted in Fig. 13a. The response toward 1.3 ppm of H_2S was found to be 25 times higher than that of other gases, confirming the high selectivity of the suggested sensor. This high selectivity might be explained as follows: nickel ferrite had a strong interaction with sulfur-containing compounds like H_2S. When target gas molecules are exposed to the sensing layer surface, the sulfur from H_2S can bond with Ni ions, increasing the sensitivity and the selectivity. Four similar pulses, as depicted in Fig. 13b, of $NiFe_2O_4$ gas response toward 1.3 ppm of H_2S at 200 °C, show the good repeatability of the fabricated sensor. Fig. 13c reported that nickel ferrite sensor response in the range of 0.126 to 5.04 ppm increased linearly, exhibiting higher sensitivity even at lower gas concentrations. As displayed in Fig. 13d, the suggested sensor had good stability after testing it toward 1.3 ppm of H_2S during 3 months with a step of 15 days.

Fig. 14 shows a comparison between the $NiFe_2O_4$ response toward 1.3 ppm of H_2S and 1 ppm of CH_2O at various temperatures from 150 to 400 °C with a step of 50 °C. At all working temperatures, the sensor response toward formaldehyde is found to be weak. At low temperatures, CH_2O gas adsorption could not excite a redox reaction because of low energy. At high temperatures, formaldehyde could be desorbed before the sensing operation occurred. In contrast, the sensor response

Table 3 Comparison of $NiFe_2O_4$ sensor toward H_2S with other metal oxides gas sensors

Material	H_2S (ppm)	Operating temp (°C)	Response	Response/recovery (s)	Reference
$NiFe_2O_4$ nanoparticles	5	200	90	10/170	This work
$NiFe_2O_4$ nanostructures	10	200	63	18/150	18
$NiFe_2O_4$ thin film	20	250	48	30/210	19 and 40
$NiFe_2O_4$-based sensors (various morphologies)	5–50	150–300	40–80	—	45
$NiFe_2O_4$ nanomaterials (review data)	1–10	150–250	50–85	—	13

toward H_2S was very high at low operating temperatures. Increasing temperature results in a gas response reduction, indicating that H_2S molecules reacted well at low temperatures.

As reported in Table 3, the fabricated sensor based on nickel ferrite nanoparticles showed a high response (90) toward low H_2S concentration (5 ppm) compared to most sensors suggested in the table.[48] The response and recovery times of $NiFe_2O_4$ sensors are found to be faster than those of other metal oxide sensors.[13,18,19,49,50]

To evaluate the repeatability of the sensor fabrication, five sensors were prepared in independent batches and tested under identical conditions (200 °C, 1.3 ppm H_2S). As shown in Fig. 15, the sensor responses are highly consistent, with a mean value of 31 and a low relative standard deviation (RSD) of 1.12%. This result demonstrates the excellent reproducibility and reliability of the fabrication process, highlighting the potential of the sensor for practical applications.

3.7. H_2S sensing mechanism

The gas detection mechanism of the nickel ferrite sensor is based on the electric resistance change because of oxygen species adsorption and H_2S interaction with the sensing layer surface. Depending on operating temperature, when the sensor was exposed to air as depicted in Fig. 16a, oxygen species are generated after the adsorption on the surface. The adsorbed oxygen species had an important role in gas sensing performance. In fact, they trapped electrons from the sensor surface, generating a depletion layer with high thickness. As a result, an increase in potential barrier height was happened yielding to resistance. The adsorbed oxygen sensing layer surface is subject to the equations situated below:[51]

$$O_2(gas) \leftrightarrow O_2(ads) \quad (3)$$

$$O_2(ads) + e^- \leftrightarrow O_2^- \quad (4)$$

$$O_2^- + e^- \leftrightarrow 2O^- \quad (5)$$

$$O^- + e^- \leftrightarrow O^{2-} \quad (6)$$

When the H_2S gas was exposed on the sensing layer surface, as shown in Fig. 16b, the target gas, as a reducing gas, reacted with adsorbed oxygen species and restored electrons to the conduction band, leading to a decrease in resistance. The reduction of resistance during H_2S gas exposure is due to a reduction in the thickness of the depletion region as well as the height of the potential barrier. The reaction can be described by the following equation:[52]

$$H_2S(g) + 2O_{(ads)}^- \rightarrow H_2(g) + SO_2(g) + 2e^- \quad (7)$$

3.8. Effect of humidity on sensing performance

The influence of relative humidity on the sensing performance of the $NiFe_2O_4$ sensor was investigated (Fig. 17). The sensor

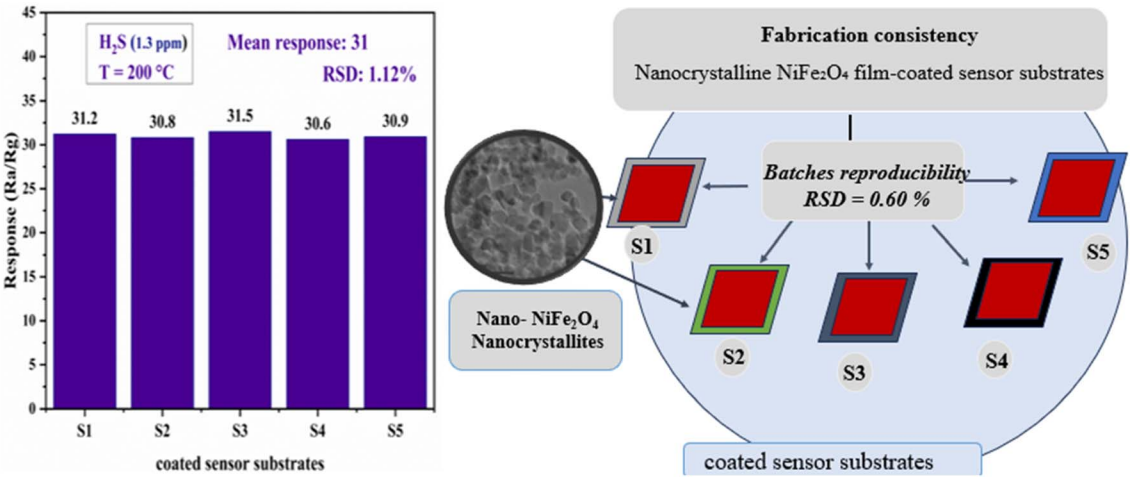

Fig. 15 Sensor response across 5 independent batches.

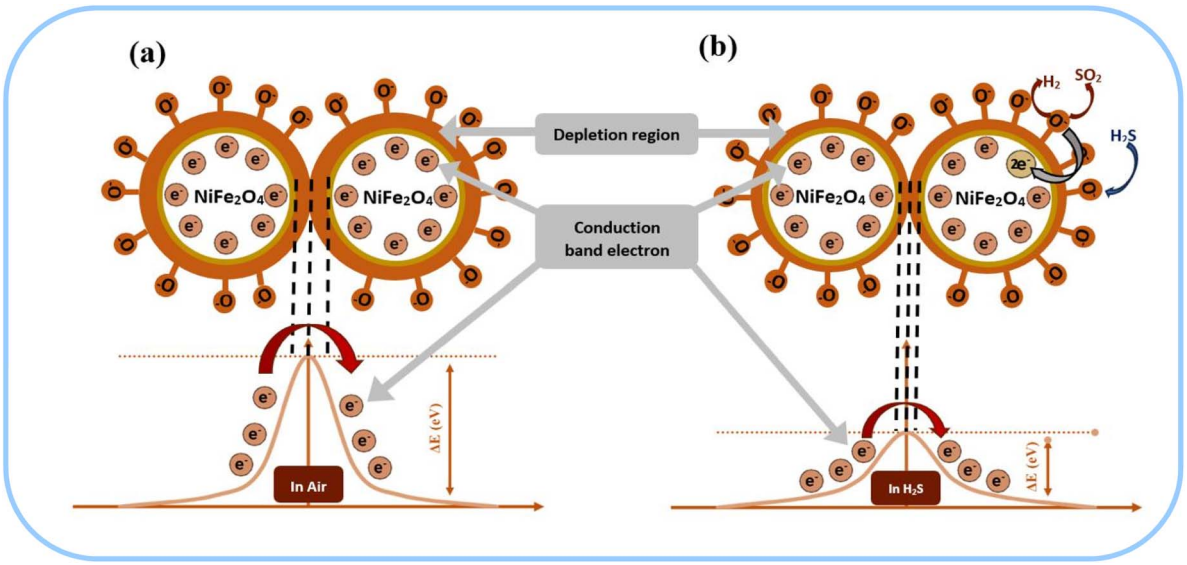

Fig. 16 Gas sensing mechanisms (a) without and (b) with H_2S gas.

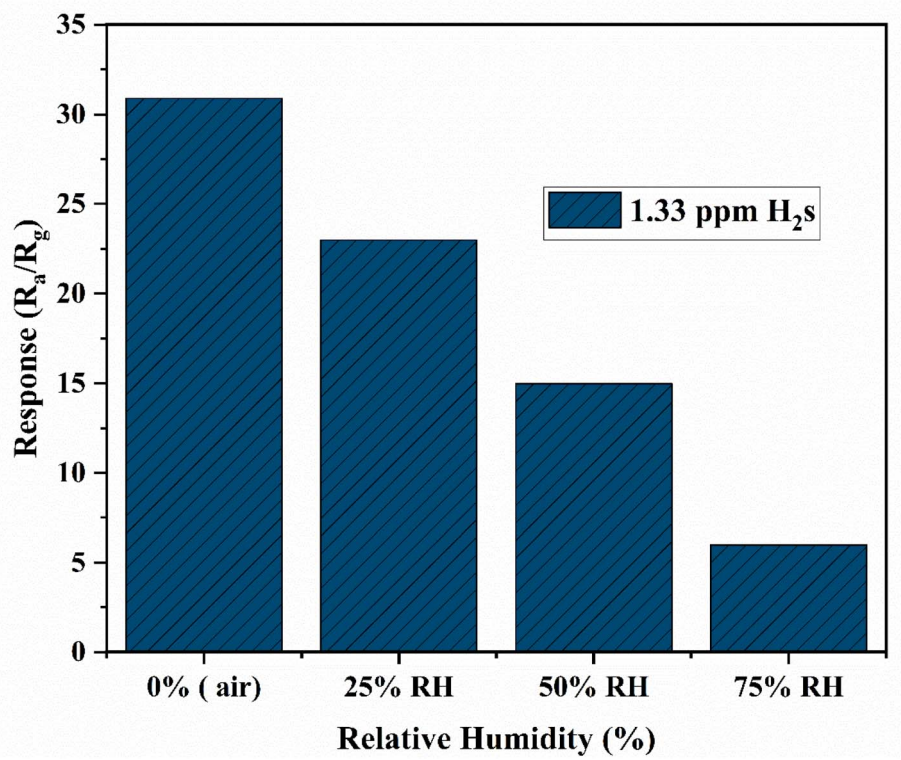

Fig. 17 Effect of relative humidity on the H_2S sensing response of $NiFe_2O_4$ sensor.

response decreases as relative humidity increases from 0% to 75%. This behavior is attributed to competitive adsorption between water molecules and oxygen species on the sensor surface. At high humidity levels, H_2O molecules occupy active sites and form hydroxyl groups, reducing the amount of chemisorbed oxygen species (O_2^-, O^-) involved in the sensing reaction. Furthermore, the formation of a water layer on the surface can impede gas diffusion. Consequently, the interaction between H_2S gas and the sensing material is weakened, leading to a decrease in the sensor response. Despite this reduction, the sensor maintains a detectable response even at high humidity levels, indicating its potential for practical applications.[53]

4. Conclusion

In this work, $NiFe_2O_4$ nanoparticles were successfully synthesized and investigated as a chemiresistive sensor for H_2S detection. Structural analysis confirmed the formation of

a cubic spinel phase, while morphological and BET results revealed a mesoporous structure with a relatively high specific surface area, providing abundant active sites for gas adsorption and facilitating efficient gas diffusion. XPS analysis provided direct insight into the sensing mechanism, confirming the interaction between H_2S molecules and the sensor surface. The appearance of sulfur-related species, the decrease in adsorbed oxygen species, and the slight shift in Ni 2p peaks demonstrate that the sensing process is governed by surface redox reactions involving Ni active sites and chemisorbed oxygen species.

The sensor exhibited excellent sensing performance, including a high response of 90 toward 5 ppm H_2S at an optimal operating temperature of 200 °C, along with a fast response time of 10 s. In addition, the sensor demonstrated good selectivity against interfering gases and maintained stable performance over an extended period. The repeatability tests showed a low relative standard deviation (RSD) of 1.12%, confirming the high reproducibility of the fabrication process.

The influence of humidity was also investigated, revealing a decrease in response at higher relative humidity due to competitive adsorption of water molecules. Despite this effect, the sensor retained a measurable response, indicating its potential applicability under realistic environmental conditions.

Overall, the combination of high sensitivity, fast response, good reproducibility, and supported sensing mechanism highlights the potential of $NiFe_2O_4$ as a promising material for efficient H_2S gas sensing. Future work will focus on improving humidity resistance and validating the sensor performance under real environmental conditions.

Compliance with ethical standard

All authors declare that the presented work was original research that has not been published previously, and not under consideration for publication elsewhere, in whole or in part.

Conflicts of interest

Authors have a responsibility to disclose interests that might appear to affect their ability to present data objectively. Readers will benefit from transparency, including knowing authors' and contributors' affiliations and interests. Sources of funding for research were disclosed.

Data availability

The data used to support the findings of this study are available from the corresponding author upon request.

Acknowledgements

This work was supported and funded by the Deanship of Scientific Research at Imam Mohammad Ibn Saud Islamic University (IMSIU) (grant number IMSIU-DDRSP2602).

References

1 M. S. Aminuddin, M. A. Bustam and K. Johari, *RSC Sustainability*, 2024, **2**(4), 757–803.
2 S. Su, Z. Zhang, J. Chen, Y. Chen, X. Cao, S. Yan and L. Chen, *J. Hazard. Mater.*, 2025, **493**, 138389.
3 M. Si, Y. Wang, R. Mei, X. Zhao, Q. Yuan, L. Fu and L. Chen, *J. Hazard. Mater.*, 2024, **480**, 136247.
4 Z. Zhang, Z. Chen, S. Wang, C. Qu and L. Chen, *ACS Appl. Mater. Interfaces*, 2014, **6**(9), 6300–6307.
5 S. Batterman, A. Grant-Alfieri and S.-H. Seo, *Crit. Rev. Toxicol.*, 2023, **53**(4), 244–295.
6 T. A. Safeera, M. S. Mozumder, E. I. Anila, G. Jose and A.-H. I. Mourad, *Mater. Today Commun.*, 2026, **51**, 114915.
7 Z. Cai and H. Kim, *npj 2D Mater. Appl.*, 2025, **9**(1), 66.
8 M. Zhu, H. Zhang, S. Zhang, H. Yao, X. Shi and S. Xu, *Materials*, 2025, **18**(2), 451.
9 M. Ghasemi, J. V. Embden, B. Jia and X. Wen, *EES Sol.*, 2025, **1**(4), 502–518.
10 Y. Masuda, *Sens. Actuators, B*, 2022, **364**, 131876.
11 N. Mustapha, B. B. Abdelaziz, M. Benamara and M. Hjiri, *Nanomaterials*, 2025, **15**(21), 1609.
12 M. A. Kareem, H. A. Shittu, A. Aremu, I. T. Bello, M. I. Nemufulwi, B. I. Adamu and M. S. Dhlamini, *Mater. Today Nano*, 2026, **33**, 100788.
13 R. Zhang, C. Qin, H. Bala, Y. Wang and J. Cao, *Nanomaterials*, 2023, **13**(15), 2188.
14 H. Soni, R. Acevedo, N. Singh, P. Sharma and Z. Ajzan, *E3S Web Conf.*, 2024, **588**, 02011.
15 I. Soudani, F. N. Almutairi, I. Chaabane, A. Oueslati, A. Aydi and K. Khirouni, *J. Phys. Chem. Solids*, 2025, **201**, 112631.
16 N. Van Hoang, P. H. Phuoc and N. V. Hieu, *Mater. Chem. Phys.*, 2025, **344**, 131117.
17 Ö. N. Avcı, L. Sementa and A. Fortunelli, *ACS Catal.*, 2022, **12**(15), 9058–9073.
18 X. Wang, X. Li, G. Zhang, Z. Wang, X.-Z. Song and Z. Tan, *Nanomaterials*, 2021, **11**(2), 297.
19 L. Zhang and W. Jiao, *Sens. Actuators, B*, 2015, **216**, 293–297.
20 S. Uma, D. Vignesh and M. K. Shobana, *Sens. Actuators, B*, 2025, **425**, 136950.
21 D. J. Dmonte, A. Bhardwaj, M. Wilhelm, T. Fischer, I. Kuřitka and S. Mathur, *Micromachines*, 2023, **14**(3), 644.
22 P. Jagtap and M. Laad, *Discover Mater.*, 2025, **5**(1), 184.
23 X. Wang, J. Zhang, Y. Wang, Y. Shen, Y. Zhang, Y. Zhang and N. Zhou, *Biosens. Bioelectron.*, 2025, **285**, 117580.
24 S. Ghaderahmadi, M. Kamkar, N. Tasnim, M. Arjmand and M. Hoorfar, *New J. Chem.*, 2021, **45**(38), 17727–17752.
25 Q. Liu, Y. Liu, Q. Wan, Q. Lu, J. Liu, Y. Ren and Y. Luo, *Anal. Chem.*, 2023, **95**(14), 5920–5926.
26 M. Si, Y. Wang, R. Mei, X. Zhao, Q. Yuan, L. Fu and L. Chen, *J. Hazard. Mater.*, 2024, **480**, 136247.
27 V. R. Naganaboina and S. G. Singh, *Chem. Phys. Rev.*, 2023, **4**(2), 021306.
28 H. Q. Alijani, S. Iravani, S. Pourseyedi, M. Torkzadeh-Mahani, M. Barani and M. Khatami, *Sci. Rep.*, 2021, **11**(1), 17431.

29 K. Vepulanont, S. Sa-Nguanprang, S. Buapoon, T. Bunluesak, P. Suebsom, K. Chaisong and T. Chanadee, *J. Australas. Ceram. Soc.*, 2021, **9**(2), 639–651.
30 I. Soudani, K. B. Brahim, A. Oueslati, H. Slimi, A. Aydi and K. Khirouni, *RSC Adv.*, 2022, **12**(29), 18697–18708.
31 I. Soudani, N. Weslati, S. Znaidia, A. Oueslati, A. Aydi and K. Khirouni, *RSC Adv.*, 2025, **15**(33), 26873–26885.
32 S. Dolabella, A. Borzì, A. Dommann and A. Neels, *Small Methods*, 2022, **6**(2), 2100932.
33 J. Li, Y. Chen, Q. He, X. Xu, H. Wang, C. Jiang and C. T. Liu, *Proc. Natl. Acad. Sci. U. S. A.*, 2022, **119**(25), e2200607119.
34 P. Liu, J. Wang, H. Jin, M. Ge, F. Zhang, C. Wang and N. Dai, *RSC Adv.*, 2023, **13**(4), 2256–2264.
35 Y. Tang, W. Wu, B. Wang, X. Dai, W. Xie, Y. Yang and Y. Fu, *Sens. Actuators, B*, 2020, **325**, 128742.
36 Y. Tang, W. Wu, B. Wang, X. Dai, W. Xie, Y. Yang and Y. Fu, *Nat. Commun.*, 2024, **15**(1), 6154.
37 H. Hu, X. Ma, Y. Wang, Z. Cheng, C. Kong, Q. Lei and E. Liu, *Adv. Sustainable Syst.*, 2026, **10**(2), e01719.
38 T. Yang, M. Boepple, A. Hémeryck, A. Jay, S. Karwounopoulos, U. Weimar and N. Barsan, *Angew. Chem., Int. Ed.*, 2025, **64**(23), e202504696.
39 Q. Hu, X. Lu, T. Gao, J. Zhang, Z. Dong, Z. Ma and J. Xu, *Sens. Actuators, B*, 2024, **414**, 135852.
40 S. Tresintsi, K. Simeonidis, N. Pliatsikas, G. Vourlias, P. Patsalas and M. Mitrakas, *J. Solid State Chem.*, 2014, **213**, 145–151.
41 M. Hjiri, N. H. Alonizan, M. M. Althubayti, S. Alshammari, H. Besbes and M. S. Aida, *J. Mater. Sci. Mater. Electron.*, 2019, **30**(16), 15379–15387.
42 N. Wang, R. X. Wang, Z. J. Li, R. Liu, H. Gao, H. Y. Chen and H. D. Zhang, *ACS Appl. Nano Mater.*, 2023, **6**(16), 15063–15072.
43 P. H. Phuoc, N. V. Hoang and N. V. Hieu, *Ceram. Int.*, 2026, **52**(1), 398–411.
44 N. Van Hoang, N. T. Hiep, N. M. Hung, C. V. Nguyen, P. T. Hung, P. D Hoat and Y. W. Heo, *J. Alloys Compd.*, 2023, **936**, 168276.
45 N. Van Hoang, N. T. Hiep, N. M. Hung, C. V. Nguyen, P. T. Hung, P. D. Hoat and Y. W. Heo, *J. Alloys Compd.*, 2023, **936**, 168276.
46 D. G. Jung, J. Lee, J. B. Kwon, B. Maeng, H. K. An and D. Jung, *Micromachines*, 2022, **13**(10), 1609.
47 P. Ghosh, A. Mukherjee, M. Fu, S. Chattopadhyay and P. Mitra, *Phys. E Low-dimens. Syst. Nanostruct.*, 2015, **74**, 570–575.
48 W. Du, X. Su, H. Yang, S. Dong, L. Chen, J. Shang and N. Wu, *Ceram. Int.*, 2024, **50**(22), 47939–47948.
49 S.-K. Tong, P.-W. Chi, S.-H. Kung and D.-H. Wei, *Sci. Rep.*, 2018, **8**(1), 1338.
50 S. R. Ananda, L. Kumari and M. M V, *Appl. Phys. A*, 2022, **128**(8), 669.
51 E. Ciftyurek, Z. Li and K. Schierbaum, *Sensors*, 2022, **23**(1), 29.
52 A. Ievtushenko, O. Khyzhun, I. Shtepliuk, O. Bykov, R. Jakieła, S. Tkach and G. Lashkarev, *J. Alloys Compd.*, 2017, **722**, 683–689.
53 A. Aziz, M. Shah, S. G. Khattak, Y. Muhammad and H. Hassan, *Mater. Sci. Eng., B*, 2024, **307**, 117519.